XXXVI Ibero-Latin American Congress on Computational Methods in Engineering
CILAMCE
Rio de Janeiro, 22-25 Nov 2015

VISUALIZING MORSE FLOWS AND ELLIPTIC UMBILIC CATASTROPHES IN N-ROLL MILL FLUIDS SIMULATED BY SMOOTHED PARTICLE HYDRODYNAMICS

Leandro Tavares da Silva[1]

Gilson Antonio Giraldi[2]

leandros@lncc.br

gilson@lncc.br

[1]Federal Center of Technology Education Celso Suckow da Fonseca

25620-003, Rio de Janeiro, Petrópolis, Brazil

[1,2]National Laboratory for Scientific Computing

25651-075, Rio de Janeiro, Petrópolis, Brazil

Abstract. *Smoothed Particle Hydrodynamics (SPH) is a meshfree, Lagrangian method which discretizes Navier-Stokes equations using a particle systems and interpolation theory. On the other hand, in the 1970's the René Thom's work in structural stability of dynamical systems allows the born of the subject now known as catastrophe theory. The remarkable consequence of such development is that, in same contexts, the system can be locally described by one of eleven standard forms named the elementary catastrophes. That is the case of the N-roll mill apparatus where N symmetrically placed rollers are surrounding by a fluid and they rotate at constant angular velocities. Qualitative analysis of the flow patterns have been performed in the context of catastrophe theory using frames extracted from experimental realizations. In this paper we simulate the N-roll mill flows, for $N = 2, 4, 6$ using the SPH technique. We analyze, by computational experiments, the structural stability of the stream functions respect to the roll velocities and artificial viscosity for two dimensional flows. The analysis is supported by quantitative results, steered by the Morse and catastrophe theories, as well as visual inspection of the flow patterns.*

Keywords: *Smoothed Particle Hydrodynamics, Catastrophe Theory, N-Roll Mill Flow, Stream Function*

1 INTRODUCTION

The majority of fluid simulation methods use 2D/3D mesh based approaches that are mathematically motivated by the Eulerian methods of Finite Element (FE) and Finite Difference (FD), in conjunction with Navier-Stokes equations of fluids (Hirsch, 1988). More recently, meshfree methods like Smoothed Particle Hydrodynamics (SPH) (Liu and Liu, 2003), Moving Particle (Kim et al., 2014), and Moving-Particle Semi-Implicit (Ataie-Ashtiani and Farhadi, 2006), have been applied. Among these techniques the SPH has the advantage of been a general one due to its capabilities to simulate a widely range of natural phenomena (Monaghan, 2012).

The SPH method was originally invented to solve astrophysical problems in three dimensional open space (Gingold and Monaghan, 1977; Monaghan, 1992). It is a meshfree, Lagrangian method which represents the fluid as a particle systems and computes fluid flow fields using interpolation functions, named kernels. Basically, field quantities are only defined at the particle locations but they can be evaluated anywhere in space using radial symmetrical smoothing kernels. Numerical and error analysis were performed in order to construct analytical kernels to obtain a n-th order approximation schemes (Liu et al., 2003). Also, variational formulations of SPH have been presented to provide useful frameworks to address conservation properties, like linear and angular momentum preservation (Bonet and Lok, 1999). Since its invention , SPH has been extensively studied and extended to address scientific and engineering problems in material science, free surface flows, explosion phenomena , heat transfer, mass flow and many other applications (Monaghan, 2012).

In this paper we focus on 2D incompressible flows modeled through Navier-Stokes equations and simulated using the SPH technique. For these fluids we can demonstrate the existence of a function $\phi : U \subset \mathbb{R}^2 \to \mathbb{R}$, where U represents the fluid domain, named stream function, which defines the stream lines and the velocity field of the fluid (Girault and Raviart, 1986). On the other hand, almost incompressible flows presents small fluctuations of the fluid volume which we postulate that correspond to small perturbations of the stream function. Besides, there are parameters related to boundary conditions that control physical and topological aspects of the stream functions. So, the fluid evolution shall be represented by a r-parameter family of a perturbed stream function. If we can count with some structural stability (insensitivity to small perturbations) then it makes sense to set up conditions for equivalence of stream functions and equivalence of the corresponding flows. In this avenue, the critical points of the stream function and its sensitivity to parameters variation and perturbations, which is part of catastrophe theory, for more details and other applications (Poston and Stewart, 1978), become also a fundamental issue for qualitative analysis of the flow.

Catastrophe theory originated with the efforts of René Thom in the 1970s (Thom, 1975). The key idea of this field is to apply topological theory of dynamical systems to model abrupt changes in natural phenomena when changing the parameters that appear in the equations. Catastrophe theory focuses on degenerate critical points of a family of functions $f : \mathbb{R}^n \times \mathbb{R}^r \to \mathbb{R}$ that depends on n real (state) variables and r control parameters.

The degenerate points place the centers for particular geometric structures named catastrophes. If the null eigenspace of the Hessian in a critical point $\mathbf{x}_0$ has dimension $1 \leq l \leq 2$ and $1 \leq r \leq 5$, then there are only eleven generic catastrophes. The corresponding functional forms define standard expressions into which the Taylor series around the degenerate critical points can be transformed by diffeomorphisms (Gilmore, 1981). Catastrophe theory has been applied in thermodynamics (Gilmore, 1981), stability analysis of black holes in generalized theories of gravity (Tamaki et al., 2003), structural mechanics (Awrejcewicz and Anatolevich, 2008), control and equilibrium theory (Loi and Matta, 2011), stability analysis in fluids (Poston and Stewart, 1978), reliability analysis (Kun et al., 2010), theoretical biology (Aihara and Suzuki, 2010), among others (Poston and Stewart, 1978).

In this paper we take a known experimental set up, the N-roll mill apparatus (Berry and Mackley, 1977), and reproduce it by computer simulation using SPH. The effect is similar to a catastrophe machine in the sense that standard catastrophe forms appear when changing the parameters involved (Poston and Stewart, 1978). The implementation of the boundary conditions in the rolls is simple in the SPH technique framework, which is a motivation for its application in the N-roll mill problem. The N-roll mill set up consists of N rollers which are surrounding by a fluid. The rollers are symmetrically placed and they rotate with constant angular velocities. Also, in our simulation the fluid domain is a rectangular region $U \subset \mathbb{R}^2$ and, consequently, we add boundary conditions. Therefore, we do not have a situation with simplified governing mechanisms that allow local analysis around critical points using only direct processes, like perturbations and Taylor series. Also, we do not perform explicit calculation of equivalence between flow patterns and elementary catastrophes. Instead, we simulate the N-roll mill flows, for $N = 2, 4, 6$ using the SPH technique. The obtained result is used to generate the stream lines patterns by fitting a generic stream function model. Next, qualitative analysis of the flow patterns is performed in the context of catastrophe theory and Morse functions. We analyze the structural stability of such structures respect to the rolls velocities and a numerical parameter (artificial viscosity), for two dimensional flows. The obtained flow patterns are compared with frames extracted from experimental realizations and analytical approximations (Berry and Mackley, 1977), in order to validate our simulation scheme.

The contributions this work are two-fold. Firstly, we develop a SPH simulation framework for the N-roll mill problem. Secondly, we demonstrate the power of the application of catastrophe theory in the understanding of fluid flows simulated with SPH frameworks. Up to the best of our knowledge, this is the first work that uses such combination in a systematic procedure.

The paper is organized as follows. In section 2 we review the catastrophe theory. Section 3 presents basic elements in CFD and stream function theory. Section 4 describes the SPH method and its application for fluid simulation. In section 5 we discuss the classification of $2D$ flows nearby critical points of the stream function. These mentioned sections assemble the theoretical elements that will steer the computational experiments presented on section 6. Conclusions and future directions for this work are given on section 7.

2 CATASTROPHE THEORY

In this section we present fundamental elements behind catastrophe theory based on (Poston and Stewart, 1978; Gilmore, 1981). We consider smooth functions $f : \mathbb{R}^n \to \mathbb{R}$; that is, functions that can be represented by its Taylor series about a point $\mathbf{x}_0 \in \mathbb{R}^n$. In what follows we interchange the notations for partial derivatives $\partial f / \partial x$ and f_x as convenient.

The notion of diffeomorphism is a fundamental element in the catastrophe theory. We shall consider maps $f : U \subset \mathbb{R}^n \to \mathbb{R}^n$, where U is an open set in $\mathbb{R}^n$ respect to the topology of open disks. If we suppose that there is an open set $V \subset \mathbb{R}^n$ such that $f(U) = V$, then f is a diffeomorphism provided: (a) f is smooth; (b) f has an inverse function $g : V \to \mathbb{R}^n$, such that $f \circ g = \mathbf{1}_V$ and $g \circ f = \mathbf{1}_U$; (c) g is smooth.

Given a r-parameter family of smooth functions $f : \mathbb{R}^n \times \mathbb{R}^r \to \mathbb{R}$ we say that a point $\mathbf{x}_0 \in \mathbb{R}^n$ is a critical point of f for $\mathbf{c} = \mathbf{c}_0$ if $D_{\mathbf{x}} f(\mathbf{x}_0, \mathbf{c}_0) = \mathbf{0}$; that means:

$$\frac{\partial f}{\partial x_1}(\mathbf{x}_0, \mathbf{c}_0) = \frac{\partial f}{\partial x_2}(\mathbf{x}_0, \mathbf{c}_0) = \ldots = \frac{\partial f}{\partial x_n}(\mathbf{x}_0, \mathbf{c}_0) = 0. \tag{1}$$

Also, we can compute the Hessian $H_{\mathbf{x}} f(\mathbf{x}_0, \mathbf{c}_0)$ as:

$$[H_{\mathbf{x}} f(\mathbf{x}_0, \mathbf{c}_0)]_{ij} = \frac{\partial^2 f}{\partial x_i \partial x_j}(\mathbf{x}_0, \mathbf{c}_0), \quad 1 \le i, j \le n, \tag{2}$$

and the dimension of the null space of the matrix $[H_{\mathbf{x}} f(\mathbf{x}_0, \mathbf{c}_0)]$ is called the corank of $H_{\mathbf{x}} f$ at $\mathbf{x}_0 \in \mathbb{R}^n$ for $\mathbf{c}_0 \in \mathbb{R}^r$.

We say that f has a non-degenerate critical point at $\mathbf{x}_0 \in \mathbb{R}^n$ for $\mathbf{c} = \mathbf{c}_0$ if $D_{\mathbf{x}} f(\mathbf{x}_0, \mathbf{c}_0) = \mathbf{0}$ and if $H_{\mathbf{x}} f(\mathbf{x}_0, \mathbf{c}_0)$, defined by Eq. (2), is non-singular (non-degenerate quadratic form). On the other hand, if $H_{\mathbf{x}} f(\mathbf{x}_0, \mathbf{c}_0)$ is degenerate we say the point $\mathbf{x}_0 \in \mathbb{R}^n$ that satisfies $D_{\mathbf{x}} f(\mathbf{x}_0, \mathbf{c}_0) = \mathbf{0}$ is a degenerate critical point for $\mathbf{c}_0$.

Two families $f, g : \mathbb{R}^n \times \mathbb{R}^r \to \mathbb{R}$ are said to be equivalent in an open neighborhood U of $(\mathbf{x}_0, \mathbf{c}_0)$ if there exist a diffeomorphism $e : \mathbb{R}^r \to \mathbb{R}^r$, smooth maps $y : \mathbb{R}^n \times \mathbb{R}^r \to \mathbb{R}^n$, $\gamma : \mathbb{R}^r \to \mathbb{R}$ defined on U, such that:

$$g(\mathbf{x}, \mathbf{s}) = f(y_{\mathbf{s}}(\mathbf{x}), e(\mathbf{s})) + \gamma(\mathbf{s}),$$

where $y_{\mathbf{s}}(\mathbf{x}) = y(\mathbf{x}, \mathbf{s})$is a diffeomorphism for all $(\mathbf{x}, \mathbf{s}) \in U$.

Morse Lemma for Families: Let $\mathbf{x}_0 \in \mathbb{R}^n$ be a non-degenerate critical point of a r-parameter family of smooth functions $f : \mathbb{R}^n \times \mathbb{R}^r \to \mathbb{R}$ for $\mathbf{c} = \mathbf{c}_0$. Then, f is equivalent in an open neighborhood U of $(\mathbf{x}_0, \mathbf{c}_0)$ to a Morse ℓ-saddle family of the form:

$$f(y_1(\mathbf{x}, \mathbf{c}), y_2(\mathbf{x}, \mathbf{c}), \ldots, y_n(\mathbf{x}, \mathbf{c})) = -y_1^2 - y_2^2 - \ldots - y_l^2 + y_{l+1}^2 + \ldots + y_n^2. \tag{3}$$

The concept of structural stability is fundamental when considering topological properties of functional spaces. If $f : \mathbb{R}^n \times \mathbb{R}^r \to \mathbb{R}$ is equivalent, in the above sense, to any family $f + p : \mathbb{R}^n \times \mathbb{R}^r \to \mathbb{R}$ where p is a sufficient small family (perturbation), then f is structurally stable. The power of the concept of structural stability becomes clear when considering a family of potentials $\phi : U \times \mathbb{R}^r \to \mathbb{R}$ that describes the conservative forces fields applied to a physical system. For example, suppose that we change the control parameters, generating a perturbation $\phi + p : U \times \mathbb{R}^r \to \mathbb{R}$. Thus, if ϕ is structurally stable, we expect that the system evolution will be qualitatively closer by considering ϕ or $\phi + p$ up to a diffeomorphism. Morse ℓ-saddle functions of the form of Eq. (3) are structurally stable. This is not the case for non-Morse functions; that is, functions with degenerate critical points. For function families with degenerate critical points, the following theorem is a remarkable one.

Tom's Theorem: If $\mathbf{x}_0 \in \mathbb{R}^n$ is a degenerate critical point of a r-parameter family of smooth functions $f : \mathbb{R}^n \times \mathbb{R}^r \to \mathbb{R}$ for $\mathbf{c} = \mathbf{c}_0$ then in an open neighborhood U of $(\mathbf{x}_0, \mathbf{c}_0)$ f is equivalent (in the sense explained above) to:

$$g(\mathbf{x}, \mathbf{c}) = \mathrm{Cat}(l, r) \pm y_{l+1}^2 \pm y_{l+2}^2 \pm \ldots \pm y_n^2, \tag{4}$$

where the function $\mathrm{Cat}\,(l,r)$ is called the catastrophe function, or simply, catastrophe, and l is the corank of $H_{\mathbf{x}}f\,(\mathbf{x}_0,\mathbf{c}_0)$, defined by Eq. (2).

The catastrophe function is in fact the sum of two functions:

$$\mathrm{Cat}\,(l,r) = \mathrm{CG}\,(l) + \mathrm{Pert}\,(l,r)\,. \tag{5}$$

where $CG\,(l)$ is the catastrophe germ and $\mathrm{Pert}\,(l,r)$ is a r-parameter family of polynomial functions. The list of eleven elementary catastrophes described by Thom, obtained with $1 \leq l \leq 2$ and $1 \leq r \leq 5$ in Eq. (4), is reported in (Gilmore, 1981), page 11. For our work, the fundamental one is the elliptic umbilic catastrophe $f : \mathbb{R}^2 \times \mathbb{R}^3 \to \mathbb{R}$, obtained by setting $l = 2$ and $r = 3$ in Eq. (5):

$$\mathrm{Cat}\,(2,3) \equiv f\,(x,y,a_1,a_2,a_3) = \frac{1}{3}x^3 - xy^2 - \frac{1}{2}a_1\left(x^2+y^2\right) + a_2 y - a_3 x. \tag{6}$$

where $\mathrm{CG}\,(2) = (1/3)x^3 - xy^2$ and $\mathrm{Pert}\,(2,3) = -(1/2)a_1\,(x^2+y^2) + a_2 y - a_3 x$. We have changed the notation $x_1 \to x$ and $x_2 \to y$ for simplicity.

The application of the elementary catastrophes to analyse a physical system described by a family $f : \mathbb{R}^n \times \mathbb{R}^r \to \mathbb{R}$ depends on finding the set S (manifold) of degenerate critical points, given by the solutions of Eq. (1) that produce degenerate Hessian matrix in Eq. (2). Then, we shall analyse the classes of transitions between Morse and non-Morse critical points obtained when crossing S (see section 5).

3 NAVIER STOKES EQUATIONS

In the Eulerian formulation of fluid mechanics, the governing equations of the fluid which connect the pressure p, density ρ and velocity $\mathbf{v}$ are the continuity (mass conservation) and the Navier-Stokes equations, given, respectively, by:

$$\frac{\partial \rho}{\partial t} + \nabla \cdot (\rho \mathbf{v}) = 0 \tag{7}$$

$$\rho\left(\frac{\partial \mathbf{v}}{\partial t} + \mathbf{v}\cdot\nabla\mathbf{v}\right) = -\nabla p + \mu\nabla^2\mathbf{v} + \mathbf{F} \tag{8}$$

Besides, we need a state equation for the pressure field. This equation must be chosen to model the appropriate fluid. In the case of almost incompressible liquids, the pressure p is temperature insensitive and can be approximated by $p = p(\rho)$ (Morris et al., 1997):

$$p = c^2\rho \tag{9}$$

where c is the speed of sound.

We shall observe that, by a direct application of the Chain rule we have $d\mathbf{v}/dt = \partial\mathbf{v}/\partial t + \mathbf{v}\cdot\nabla\mathbf{v}$. Therefore, the Navier-Stokes momentum equation in Eq. (8) can be written in the form:

$$\frac{d\mathbf{v}}{dt} = -\frac{1}{\rho}(\nabla p + \mu\nabla^2\mathbf{v} + \mathbf{F},) \tag{10}$$

where the derivative d/dt is called the material one.

Given a bi-dimensional domain $U \subset \mathbb{R}^2$, with fixed boundary ∂U; a stationary solution of Eq. (8), subject to incompressibility ($\nabla\cdot\mathbf{v} = 0$) and no-slip ($\mathbf{v}|_{\partial U} = \mathbf{0}$) boundary condition, can be represented by a stream function $\phi : U \to \mathbb{R}$, which has the properties:

1. Isolines of ϕ define the stream lines of the flow;
2. Fluid velocity $\mathbf{v}$ is given by:

$$\mathbf{v}(x,y) = (\phi_y, -\phi_x). \tag{11}$$

From Eq. (11), it is straightforward to show that the vorticity ($\omega = \nabla \times \mathbf{v}$) of the flow is:

$$\omega = -(\phi_{xx} + \phi_{yy}) \equiv -\nabla^2\phi, \tag{12}$$

where '$\times$' represent the usual curl operator.

In some sense, there is a one-to-one mapping between the space of stream functions and the space of $2D$ steady and incompressible flows. However, once there are parameters involved (viscosity, for instance), we in fact have a family $\phi : U \times \mathbb{R}^r \rightarrow \mathbb{R}$, which is function of state variables $(x, y) \in U$, with $U \subset \mathbb{R}^2$, and $\mathbb{R}^r$ is the control parameter space. Also, from Eq. (11), it is clear that the critical points of ϕ are the places where the flow velocity vanishes, named the stationary points of the flow. In this sense, the topology of the stream functions space determined by the Thom' catastrophes nearby critical points of ϕ gives fundamental elements for flow analysis that goes beyond the traditional flow classification nearby hyperbolic stationary points (another consequence of Morse Lemma, as we will see).

4 SPH VERSION OF FLUID EQUATIONS

The two fundamental elements in the SPH method are an interpolation kernel $W : \mathbb{R}^3 \rightarrow \mathbb{R}^+$, which is a symmetric function respect to the origin $(0, 0, 0)$, limited, with compact support, and a particle system $\mathbf{r}_i = (x_{i1}, x_{i2}, x_{i3}) \in \mathbb{R}^3$, $i = 1, 2, \ldots, M$, that represents a discrete version (sample) of the fluid. The kernel estimate of a scalar quantity A and its gradient in a point $\mathbf{r}_i \in \mathbb{R}^3$ are given by (Liu and Liu, 2003):

$$\langle A(\mathbf{r}_i)\rangle = \sum_{j=1}^{M} \frac{m_j}{\rho(\mathbf{r}_j)} A(\mathbf{r}_j) W(\mathbf{r}_i - \mathbf{r}_j, h), \tag{13}$$

$$\langle \nabla A(\mathbf{r}_i)\rangle = \sum_{j=1}^{M} \frac{m_j}{\rho(\mathbf{r}_j)} A(\mathbf{r}_j) \nabla_i W(\mathbf{r}_i - \mathbf{r}_j, h), \tag{14}$$

where $\nabla_i W(\mathbf{r}_i - \mathbf{r}_j, h)$ means $\nabla_{\mathbf{r}} W(\mathbf{r} - \mathbf{r}_j, h)$ evaluated at $\mathbf{r} = \mathbf{r}_i$, h is the smoothing length which determines the support of the kernel and $\rho(\mathbf{r}_j)$ is the density at the particle position $\mathbf{r}_j$ (Liu and Liu, 2003). Therefore, the kernel estimate of the density at the position $\mathbf{r}_i$ is:

$$\langle \rho(\mathbf{r}_i)\rangle = \sum_{j=1}^{M} m_j W(\mathbf{r}_i - \mathbf{r}_j, h), \tag{15}$$

Besides, we can show that the divergent for a vector field $\mathbf{v}$ can be computed as (Liu and Liu, 2003):

$$\langle \nabla\cdot\mathbf{v}(\mathbf{r}_i)\rangle = \sum_{j=1}^{M} \frac{m_j}{\rho(\mathbf{r}_j)} (\mathbf{v}(\mathbf{r}_j) - \mathbf{v}(\mathbf{r}_i)) \nabla_i W(\mathbf{r}_i - \mathbf{r}_j, h), \tag{16}$$

An analogous expression can be obtained by the Laplacian. From Eq. (14) and Eq. (16) we can observe that there is no need for a mesh to compute spatial derivatives. With Eq. (13)-(16), we are ready to write the discrete version of the fluid equations of section 3. For simplicity, we will remove the brackets and place a subscript i on the denoted value; that is: $\langle A(\mathbf{r}_i)\rangle \equiv A_i$ and $\langle \nabla A(\mathbf{r}_i)\rangle \equiv \nabla A_i$. We also use the notations $W_{ij} \equiv W(\mathbf{r}_i - \mathbf{r}_j, h)$ and $\rho(\mathbf{r}_j) \equiv \rho_j$. By using the material derivative for the density ($d\rho/dt = \partial\rho/\partial t + \nabla\rho \cdot \mathbf{v}$) as well as Eq. (14)-(16) we can show that the SPH version of the time derivative of the density becomes:

$$\frac{d\rho_i}{dt} = \sum_{j=1}^{M} m_j \mathbf{v}_{ij} \nabla_i W_{ij}, \tag{17}$$

where $\mathbf{v}_{ij} \equiv \mathbf{v}_i - \mathbf{v}_j$.

Now, we shall obtain the discrete version of the Navier-Stokes equation given by Eq. (10). Firstly, we will consider separately each term before to put all together. The pressure gradient could be directly computed using Eq. (14) but the obtained expression does not conserve linear momentum (Morris et al., 1997). To address this problem, we shall rewrite the pressure gradient as: $(\nabla p/\rho) = \nabla\left(p/\rho\right) + \left(p/\rho^2\right)\nabla\rho$. Then, we can use the Eq. (14) to calculate the gradients to obtain the acceleration that particle i feels due to the pressure force only:

$$\frac{d\mathbf{v}_i}{dt} = -\sum_{j=1}^{M} m_j \left(\frac{p_j}{\rho_j^2} + \frac{p_i}{\rho_i^2}\right) \nabla_i W_{ij}. \tag{18}$$

Due to numerical stability issues we follow (Liu and Liu, 2003) and use the artificial viscosity computed by:

$$\Pi^{ij} = \begin{cases} \dfrac{-2(a\varphi_{ij}c + b\varphi_{ij}^2)}{\rho^i + \rho^j}, & \mathbf{v}^{ij}\cdot\mathbf{x}^{ij} < 0 \\ 0, & \mathbf{v}^{ij}\cdot\mathbf{x}^{ij} \geq 0 \end{cases} \tag{19}$$

with:

$$\varphi_{ij} = \frac{(\mathbf{v}^{ij}\cdot\mathbf{x}^{ij})h}{\left(r_k^{ij}\right)^2 + 0.01h^2} \tag{20}$$

where a, $b\mathbf{v}^{ij} = \mathbf{v}^i - \mathbf{v}^j$, $\mathbf{x}^{ij} = \mathbf{r}^i - \mathbf{r}^j$, $r^{ij} = \|\mathbf{x}^{ij}\|$, and:

$$\mathbf{v}^i_{k+\frac{1}{2}\Delta t} = \mathbf{v}^i_{k-\frac{1}{2}\Delta t} + \Delta\mathbf{a}_i(t)t. \tag{21}$$

Actual viscous effects can be introduced in the SPH framework through a kernel version of the viscous term in Eq. (10), given by:

$$\nabla^2\mathbf{v}_i = 2.0\frac{\nu}{\rho_i}\sum_{j=1}^{N} \frac{m_j\mathbf{v}^{ij}}{\rho_j}\frac{\mathbf{x}^{ij}\cdot\nabla_i W_{ij}}{r^{ij}}, \tag{22}$$

where $\mathbf{v}^{ij}$, $\mathbf{x}^{ij}$, r^{ij}, are defined above.

Besides, we shall include repulsive boundary forces to prevent the interior particle from penetrating the boundary of the domain. In this work this is implemented using boundary particles that do not move but interact with fluid particles (Liu and Liu, 2003). Specifically, if a boundary particle $\mathbf{q}^g$ is the neighboring particle of a real particle $\mathbf{q}_k^i$ that is approaching the boundary, then the force:

$$\Gamma_k^{ig} = \begin{cases} D\left[\left(\frac{r_0}{r_k^{ig}}\right)^{n_1} - \left(\frac{r_0}{r_k^{ig}}\right)^{n_2}\right] & \frac{r_0}{r_k^{ig}} \leq 1 \\ 0 & \frac{r_0}{r_k^{ig}} > 1 \end{cases} \tag{23}$$

is applied pairwise along the centerline of these two particles, where $n_1 = 12$, $n_2 = 4$, $r_k^{ig} = \|\mathbf{x}^i - \mathbf{x}^g\|$, and r_0 is usually selected close to the initial particle spacing. The parameter D is problem dependent, and its value should be chosen with the same order of the square of the largest velocity, a,

Once the force terms are computed, the acceleration of particle i can be obtained by:

$$\mathbf{a}_i = \frac{d\mathbf{v}_i}{dt} = -\frac{\nabla p_i}{\rho_i} + \frac{1}{\rho_i}\left(\mu\nabla^2\mathbf{v}_i + \Pi^{ij} + \Gamma^{ig} + \mathbf{F}_i\right). \tag{24}$$

Thus, an integration scheme, the Leap-Frog one, is used in order to update the velocity and the position particles as follows:

$$\mathbf{v}_i^{t+\Delta t} = \mathbf{v}_i^t + \frac{\delta t}{2}\mathbf{a}_i^t, \tag{25}$$

$$\mathbf{r}_i^{t+\Delta t} = \mathbf{r}_i^t + \delta t \mathbf{v}_i^{t+\Delta t}, \tag{26}$$

where δt is the time step for the integrator.

In this work, the kernel function adopted is the quintic smoothing function:

$$W(R) = \begin{cases} (3-R)^5 - 6(2-R)^5 - 15(1-R)^5, & 0 \leq R < 1 \\ (3-R)^5 - 6(2-R)^5, & 1 \leq R < 2 \\ (3-R)^5, & 2 \leq R < 3 \\ 0, & R \geq 3 \end{cases} \tag{27}$$

where $R = \frac{\|\mathbf{r}_i - \mathbf{r}_j\|}{h}$, and h is a constant. Remarking that we used the cubic smoothing function, but the outcome was not satisfactory.

In the SPH framework to simulate the n-roll mill setup we use two types of particles: SPH particles and roll particles. The former is used to simulate the fluid while the latter are uniformly distributed along the rolls boundary and they simulate the interaction between rolls and the fluid. In the simulation pipeline, the SPH particle are processed by: (a) Compute the pressure field using Eq. (9) and the density at previous time; (b) Update the density field by integrating Eq. (17); (c) Compute the accelerations by Eq. (24); (d) Update the velocity and the position of SPH particles through Eq. (25)-(26), respectively. In our implementation rolls particles are treated like the SPH ones. However, we do not update position and velocity of rolls particles. Consequently, we only update the pressure and density at their positions in each integration step. This simple strategy simulates the idea of rigid rolls whose physical properties are not affected due to the fluid surrounding them.

5 TWO-DIMENSIONAL FLOW CLASSIFICATION

Topological techniques provide the natural framework to address the problem of classification of possible streamline structures. In fact, the elementary geometries of streamlines trajectories from stream functions in $\mathbb{R}^2$ can be classified using the Morse Lemma and the elementary Thom's catastrophes. Specifically, let $\phi : \mathbb{R}^2 \times \mathbb{R}^r \rightarrow \mathbb{R}$ be a smooth stream function family. Its Hessian respect to $\mathbf{x} = (x, y) \in \mathbb{R}^2$ is computed by Eq. (2) and, consequently, the associated eigenvalue equation is:

$$det\left(H_{\mathbf{x}}\phi - tI\right) = t^2 - t\left(\phi_{xx} + \phi_{yy}\right) + \left(-\phi_{yx}^2 + \phi_{xx}\phi_{yy}\right) = 0. \tag{28}$$

Once $H_{\mathbf{x}}\phi$ is symmetric, the solution of the Eq. (28) in a critical point $\mathbf{x}_0 \in \mathbb{R}^2$ of ϕ for $\mathbf{c}_0 \in \mathbb{R}^r$ are two eigenvalues $\lambda_1(\mathbf{c}_0), \lambda_2(\mathbf{c}_0) \in \mathbb{R}$. Hence, we have the following possibilities: (a) Local minimum: $\lambda_1(\mathbf{c}_0) > 0$, $\lambda_2(\mathbf{c}_0) > 0$; (b) Local maximum: $\lambda_1(\mathbf{c}_0) < 0$, and $\lambda_2(\mathbf{c}_0) < 0$; (c) Saddle: $\lambda_1(\mathbf{c}_0) \cdot \lambda_2(\mathbf{c}_0) < 0$; (d) Degenerate critical point: $\lambda_1(\mathbf{c}_0) \cdot \lambda_2(\mathbf{c}_0) = 0$. The first three cases are non-degenerate critical points and so are covered by the Morse Lemma (section 2) which assures that ϕ is equivalent in an open neighborhood U of $(\mathbf{x}_0, \mathbf{c}_0)$ to a family of the form:

$$\phi(\mathbf{x}, \mathbf{c}) = \lambda_1(\mathbf{c})\, y_1^2(\mathbf{x}) + \lambda_2(\mathbf{c})\, y_2^2(\mathbf{x}). \tag{29}$$

Therefore, due to the structural stability of Morse functions, the velocity field $\mathbf{v}$ in the neighborhood U can be represented by:

$$\mathbf{v} = \left(\frac{\partial\phi(\mathbf{x}, \mathbf{c}_0)}{\partial y_2}, -\frac{\partial\phi(\mathbf{x}, \mathbf{c}_0)}{\partial y_1}\right) = \left(2\lambda_2 y_2, -2\lambda_1 y_1\right),$$

and the streamline structures in U have the patterns picture in Fig. 1.

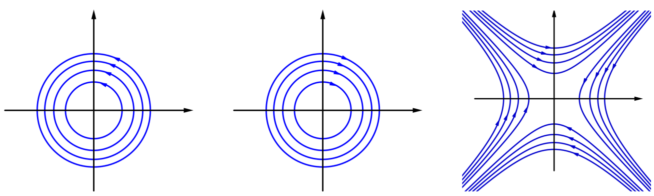

(a) Local minimum (b) local maximum (c) saddle point

Figure 1

To consider the degenerate case we must return to the velocity field $\mathbf{v}$, computed by Eq. (11), and take its derivative $D_{\mathbf{x}}\mathbf{v}$, respect to $\mathbf{x} = (x, y) \in \mathbb{R}^2$, given by:

$$D_{\mathbf{x}}\mathbf{v} = \begin{bmatrix} \phi_{yx} & \phi_{yy} \\ -\phi_{xx} & -\phi_{yx} \end{bmatrix}. \tag{30}$$

to analyse the local structure of singular points (Strogatz, 2007). Therefore, we must check the solutions of the eigenvalue equation: $\det(D_{\mathbf{x}}\mathbf{v} - tI) = t^2 - \phi_{yx}^2 + \phi_{xx}\phi_{yy} = 0$. This equation is equal to Eq. (28) if the vorticity $\omega = -(\phi_{xx} + \phi_{yy})$ is null (see Eq. (12)). Hence, the degenerate case must have two null eigenvalues and the non-degenerate singularities are covered by the case (c) above. If we consider $r = 3$ for the dimension of the control parameter space, the only possibility to deal with this case in the eleven elementary catastrophes (see (Gilmore, 1981), page 11) is the elliptic umbilic catastrophe, given by Eq. (6).

So, we shall study the critical points of the function in Eq. (6) to characterize the flow classes. In this way, the first step is to parameterize the set (manifold) of critical points of the family in Eq. (6), which is denoted $\mathcal{M}$. Following definition in Eq. (1), this is obtained by solving the pair of equations:

$$\frac{\partial f}{\partial x}(x, y, a_1, a_2, a_3) = x^2 - y^2 - a_1 x - a_3 = 0 \tag{31}$$
$$\frac{\partial f}{\partial y}(x, y, a_1, a_2, a_3) = -2xy - a_1 y + a_2 = 0. \tag{32}$$

Therefore, we can parameterize $\mathcal{M}$ using the variables (x, y, a_1) as follows:

$$\varphi(x, y, a_3) = \left(a_1, 2xy + 2a_1 y, x^2 - y^2 - a_1 x\right) = (a_1, a_2, a_3) \in M. \tag{33}$$

In order to find the degenerate critical points we shall seek for the critical points that satisfy equation:

$$\det\left[H_{\mathbf{x}} f(x, y, a_1, a_2, a_3)\right] = \det \begin{bmatrix} 2x - a_1 & -2y \\ -2y & -2x - a_1 \end{bmatrix} = 0 \tag{34}$$

which renders: $x^2 + y^2 = \frac{a_1^2}{4}$. By substituting this result in Eq. (33), we demonstrate that the two variables x and y can be use to obtain a parametric representation of the surface S that contains the degenerate critical points:

$$\varphi(x, y) = \left(\pm 2\sqrt{x^2 + y^2}, 2xy \pm 2y\sqrt{x^2 + y^2}, x^2 - y^2 \mp 2x\sqrt{x^2 + y^2}\right). \tag{35}$$

This surface is visualized in Fig. 2, immersed in the parameter space (a_1, a_2, a_3), and it is named bifurcation surface (or separatrix) due to the topological changes that happen when crossing it. In fact, we must notice that if we take a line R that crosses the surface given by Eq. (35), then we get Morse functions before crossing S, a non-Morse function for $\mathbf{q} = R \cap S$ and again Morse functions after $\mathbf{q}$. Such transitions are responsible for topological changes in the flow patterns, which justify the name separatrix or bifurcation surface for S.

As observed in (Berry and Mackley, 1977), there are some sort of topological changes in the flow family under consideration depending on the intersections between R and S. Specifically,

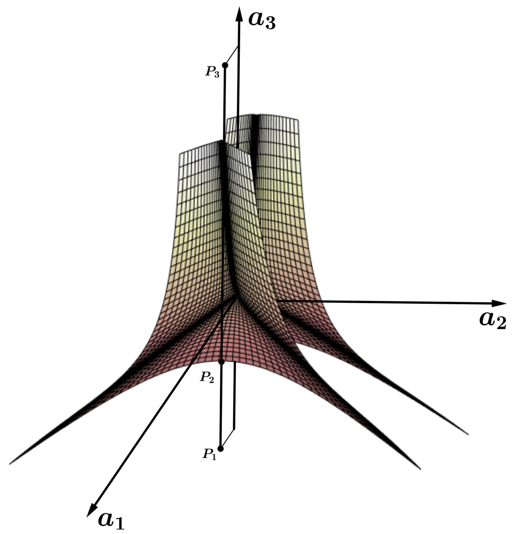

Figure 2: Bifurcation surface for the elliptic umbilic catastrophe.

let us take a line R that pierces the smooth surface S as shown in Fig. 2. Now, we take the sequence of positions $p_1 = (1.0, 0.0, -1.0)$, $p_2 = (1.0, 0.0, -0.25)$ and $p_3 = (1.0, 0.0, 1.0)$, along R, where p_1,p_3 are outside S and p_2 is over the surface S. We notice two saddles in p_1, a degenerate critical point in p_2 besides two saddles, and, finally, the topology returning to two saddles in p_3. The corresponding flow patterns are pictured on Fig. 3.(a)-(c). They are obtained by taking Eq. (6) and setting $(a_1, a_2, a_3) = p_1$, in the case of flow of Fig. 3.(a), $(a_1, a_2, a_3) = p_2$ for Fig. 3.(b), $(a_1, a_2, a_3) = p_3$ for Fig. 3.(c).

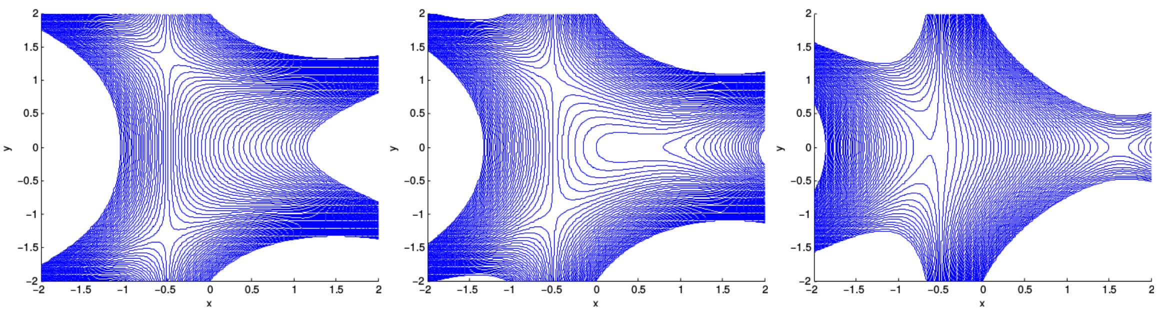

(a) (b) (c)

Figure 3: Flow topology for points (a) $p_1 = (1.0, 0.0, -1.0)$**. (b)** $p_2 = (1.0, 0.0, -0.25)$**. (c)** $p_3 = (1.0, 0.0, 1.0)$**.**

The surface given by the Eq. (35) is diffeomorphic to a double cone in the parameter space (a_1, a_2, a_3). It divides the control parameter space, $\mathbb{R}^3$ in this case, into open regions which describe functions with qualitatively different behaviors, as commented above. This will be explored in the experimental results.

6 COMPUTATIONAL EXPERIMENTS

In this section we focus on bi-dimensional fluid simulations of N-roll mill setups that allow the realization of Morse and non-Morse flows. All the simulations are performed using the SPH approach described on section 4. We validate our SPH simulation approach by comparing the simulated flows with frames extracted from experimental realizations (Berry and Mackley, 1977). The computational setup is composed by $2n$ roll mil apparatus with domain $U \subset \mathbb{R}^2$, filled by a viscous fluid. The flow visualization is implemented using the line integral convolution technique, adapted for SPH results, available in the Paraview system (Henderson and Ahrens, 2004).

We start with Morse saddles and end with the elliptic umbilic catastrophe given by Eq. (3) and Eq. (6), respectively. For the former, the analysis of the stability of the corresponding structures against parameter variation is the main goal. In the case of non-Morse flows (degenerate critical points) we explore some flow topologies that the surface in Eq. (35) defines. To perform these tasks, we shall compute the stream function from the numerical results and compare it with umbilic catastrophe in Eq. (6).

Therefore, we firstly get the fluid configuration obtained by SPH simulation performed by Eq. (25)-(26). Then, we take general forms for bi-dimensional saddles and the umbilic catastrophe given by:

$$\phi_M\left(x,y\right) = b_{20}x^2 + b_{02}y^2 + 2b_{11}xy + b_{10}x + b_{01}y + b_{00}, \tag{36}$$

$$\phi_{NM}\left(x,y\right) = b_{30}x^3 + b_{12}xy^2 + b_{20}x^2 + b_{02}y^2 + b_{10}x + b_{01}y. \tag{37}$$

Then, we fit these general forms to the SPH solution by solving the system:

$$\mathbf{v}_i = \left(\frac{\partial \phi}{\partial y}\left(x_i, y_i\right), -\frac{\partial \phi}{\partial x}\left(x_i, y_i\right)\right), \quad i = 1, 2, \ldots, M, \tag{38}$$

where $\phi = \phi_M$ or $\phi = \phi_{NM}$ and $\mathbf{v}_i$ is the velocity of particle $\mathbf{r}_i = (x_i, y_i)$ in the SPH solution. The Eq. (38) is solved through traditional least square techniques. We postulate the Eq. (36)-(37) steered by Morse Lemma and the canonical form of the umbilic catastrophe. However, we increase the dimension of parameter space to avoid biased solutions. Obviously, we are assuming the necessity of coordinates changes (diffeomorphisms) to transform Eq. (36)-(37) into the canonical forms of saddles and umbilic catastrophe.

The Fig. 4.(a)-(c) represents the computational setups used in the simulations of this section. The Fig. 4.(d)-(f) pictures the corresponding experimental plates, which show photographs of the fluid flow that is made visible in the laboratory by illuminating the regions between the rollers with a horizontal plane beam (see (Berry and Mackley, 1977) for experimental details).

For all cases, the kernel function is calculated by Eq. (27) with smoothing length $h = 0.006$. The rest density is $\rho_0 = 1261.3\ kg/m^3$, $a = b = 0.9$ in the artificial viscosity, and the simulation domain D is filled by a fluid with the glycerol viscosity ($\mu = 1.5\ Pa \cdot s^{-1}$). In the case of Fig. 4.(a), the domain dimensions are $D_x = 0.30\ m$, $D_y = 0.145\ m$ and the roller centers are placed in the points $C_1 = (0.0725, 0.07525)$ and $C_2 = (0.2175, 0.0725)$. They have radius $a = 0.03\ m$ and separation $d = 0.085\ m$. They rotate in the clockwise direction, as shown in Fig. 4.(a). The angular velocities are given by $\Omega_1 = 0.05\ rad/s$ and $\Omega_2 = 0.05\ rad/s$. The simulation uses $M = 1404$ SPH particles, each one with mass $0.03286 kg$ and initial null velocity.

In the 4-roll mill setup, pictured on Fig. 4.(b), the computational domain has dimensions $D_x = 0.30\ m$, $D_y = 0.29\ m$ and the roller centers are symmetrically placed in the points $C_1 = (0.0725, 0.0725)$, $C_2 = (0.2175, 0.0725)$, $C_3 = (0.0725, 0.2175)$, and $C_4 = (0.2175, 0.2175)$.

They have radius $a = 0.03\ m$ and separation $d = 0.085\ m$. They rotate at equal linear speeds but with alternating directions. as shown in Fig. 4.(b). The angular velocities are given by $\Omega_1 = \Omega_2 = \Omega_3 = \Omega_4 = 0.05\ rad/s$. The simulation uses $M = 2808$ SPH particles, each one with mass $0.03286kg$.

The 6-roll mill apparatus, represented on Fig. 4.(c), is simulated using a computational domain with dimensions $D_x = 0.38$, $D_y = 0.36\ m$ and the roller centers are symmetrically placed in the points $C_1 = (0.24, 0.1794)$, $C_2 = (0.2155, 0.223)$, $C_3 = (0.1655, 0.2236)$, and $C_4 = (0.14, 0.1806)$, $C_5 = (0.1645, 0.137)$, and $C_6 = (0.2145, 0.137)$. They have radius $a = 0.01\ m$ and separation $d = 0.04\ m$. They rotate with constant angular velocities but the directions will be specified later. The simulation uses $M = 5131$ SPH particles, each one with mass $0.03286kg$.

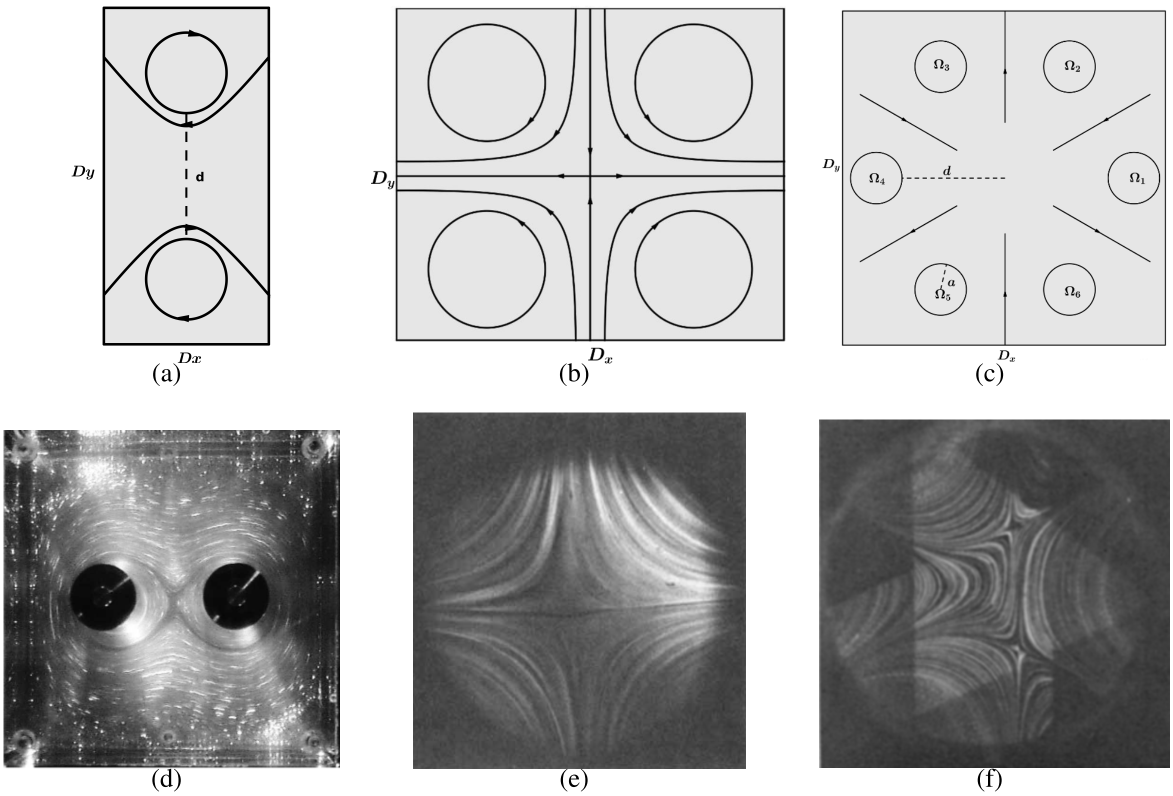

Figure 4: (a),(d) Two-roll mill scheme and experimental visualization in (Hills, 2002). (b),(e) The 4-roll setup for simulation and experimental realization in (Crowley et al., 1976). (c),(f) The 6-roll mill apparatus scheme and experimental realization in (Berry and Mackley, 1977).

6.1 Morse Flows

A stream functions with a saddle point generates saddle flows like in Fig. 1.(c), as a consequence of the stream function theory summarized in the end of section 3. These flows can be experimentally realized using the two and four-roll mil apparatus that are pictured in Fig. 4.(a),(b), respectively.

So, we perform numerical simulation of the 2 and 4-roll mill experiments pictured in Fig. 4, using the physical and numerical parameters cited above. For both the 2 and 4 cases the

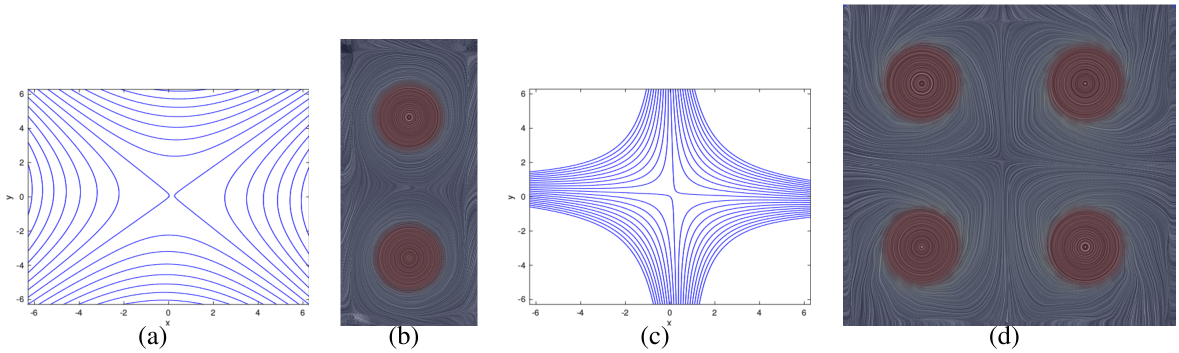

Figure 5: (a) Saddle obtained through 2-roll mill simulation. (b) LIC visualization of the 2-roll mill velocity field. (c) Saddle computed for the 4-roll mill simulation. (d) LIC visualization of the 4-roll velocity field.

angular velocities have the same absolute value and the rolls rotate according to Fig. 4.(a),(b). The flows given by the solution of the system in Eq. (38) are shown on Fig. 5.(a),(c). The Fig. 5.(b),(d) pictures the LIC visualization of the velocity field. We observe a suitable agreement between the experimental plates and the numerical flows visualization shown in Fig. 4.(d),(e) and 5.(b),(d), respectively. Besides, the streamlines patterns in Fig. 5.(a),(c) have the saddle Morse topology, as expected. These facts confirm the correctness of our 2 and 4-roll SPH implementations.

However, we must be aware about the fact that the SPH implementation undergoes issues about boundary effects, numerical parameters and viscosity that intrude upon the numerical simulation results. As a consequence instead of thinking about a stream function we shall consider a r-parameter family of stream functions. However, we expect that sufficiently small changes in the conditions under which the computation is carried out should not significantly affect the result. We can postulate such things if we can count with structural stability.

The stability of Morse saddles shows up clearly with the 2-roll mill when simulating it with angular velocities perturbed by $\Delta\Omega = 0.001$. Another sequence of computational experiments are performed with the artificial viscosity in Eq. (19) scaled by $a + \Delta a$ and $b + \Delta b$, where $a = b$ and $\Delta a = \Delta b = -0.5$.The results are shown in Fig. 6 and the preservation of the flow topology can be confirmed.

The 4-roll mill flows belong to a class of flows where $2n$ alternately outgoing and ingoing streamlines issue symmetrically from a non-degenerate critical point. By using complex variable methods, it can be demonstrate that the stream function in a disc-shaped region fitted between the rollers is (Berry and Mackley, 1977):

$$\phi = \frac{\gamma}{n} Re\left(x + iy\right)^{n}. \tag{39}$$

In the case of the 4-roll mill we shall set $n = 2$ in Eq. (39) to obtain $\phi\left(x, y\right) = \left(\gamma/2\right) Re\left(x^2 - y^2 + 2ixy\right) = \left(\gamma/2\right)\left(x^2 - y^2\right)$. Therefore, there must be a saddle point between the rolls, with a more general model for it being a stream function given by Eq. (36). The flow (isolines) pattern shown in Fig. 5.(c) agrees with this fact up to rotations.

Likewise in the case of two rolls, we perturb the angular velocity by $\Delta\Omega = 0.001$ and the artificial viscosity parameters by $\Delta a = \Delta b = -0.5$, and, perform the SPH simulation of the

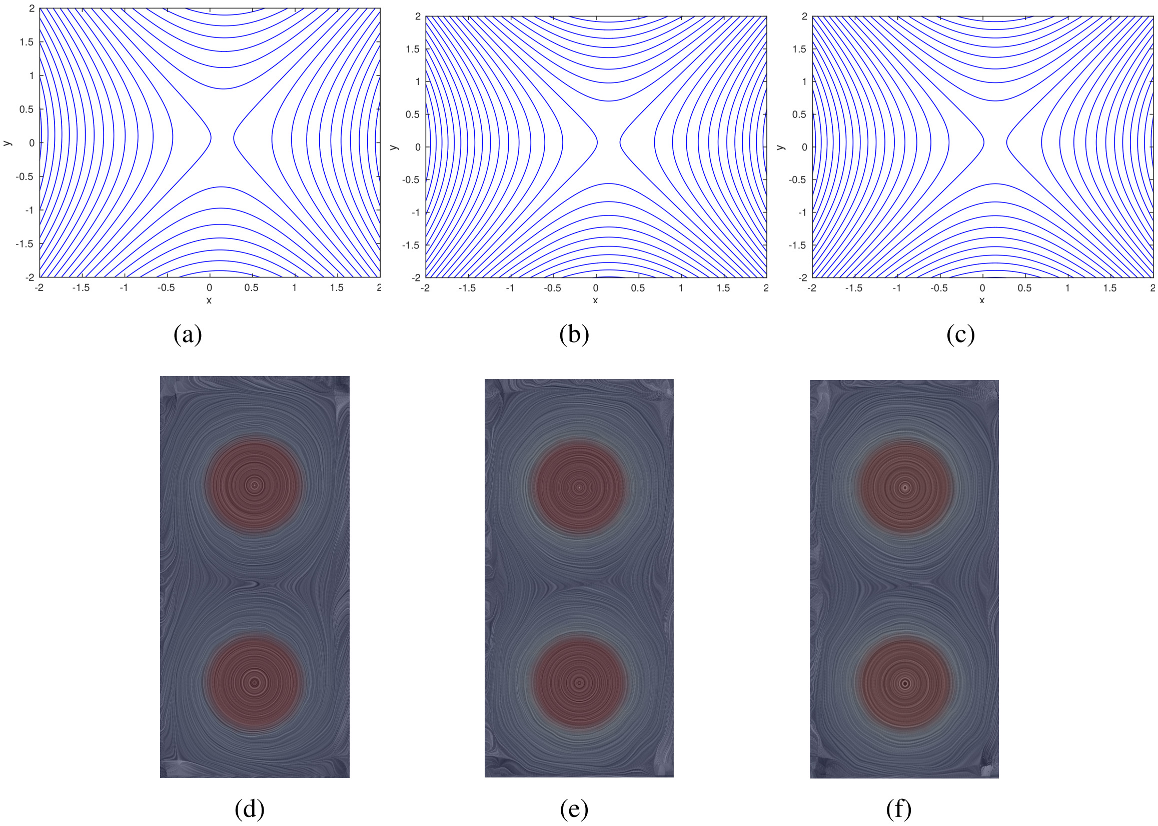

Figure 6: Two-roll mill streamlines pattern and LIC visualization using: (a),(d) $\Omega_1 = \Omega_2 = 0.051$**. (b),(e)** $\Omega_1 = \Omega_2 = 0.05$ **and** $a = b = 0.4$**. (c)-(f)** $\Omega_1 = \Omega_2 = 0.051$ **and** $a = b = 0.4$**.**

fluid. The Fig. 7 shows the obtained streamlines patterns and the LIC visualization. Like in the 2-roll case, we also observe the insensitivity to small perturbations of the angular velocity and artificial viscosity. The success of the saddle point to approximate the flow owes much to the structural stability of Morse functions; small perturbations in the simulation parameters generate perturbed SPH solution but with topology preservation.

6.2 The Six-Roll Mill: Degenerate Flow

If we set $n = 3$ in Eq. (39) we obtain $\phi(x, y) = (\gamma/3)(x^3 - 3xy^2)$, which corresponds to the germ of the elliptic umbilic catastrophe in Eq. (6), scaled by a factor γ. This is an irrotational flow ($|\nabla^2\phi| = ||\nabla \times \mathbf{v}|| = 0$), likewise the flows described in section 6.1. This suggests that the universal unfolding for the umbilic catastrophe contains the 'missing' linear and quadratic terms in x and y, and it is plausible on physical grounds that these terms correspond to the addition to the singular flow of a uniform translational flow with velocity defined by a_2 and a_3 and a uniform vorticity proportional to $a_3\mathbf{z}$, for more details, see (Poston and Stewart, 1978; Berry and Mackley, 1977).

Therefore, we could cast the six-roll mill flow in the elliptic umbilic catastrophe scenario (section 5). The apparatus to check this claim is the six-roll one described on Fig. 4.(c). Following (Berry and Mackley, 1977) we consider three angular velocities for the rolls, say $\Omega_3 = \Omega_5 = \Omega_I$, $|\Omega_1| = |\Omega_4| = \Omega_{II}$, $\Omega_2 = \Omega_6 = \Omega_{III}$.

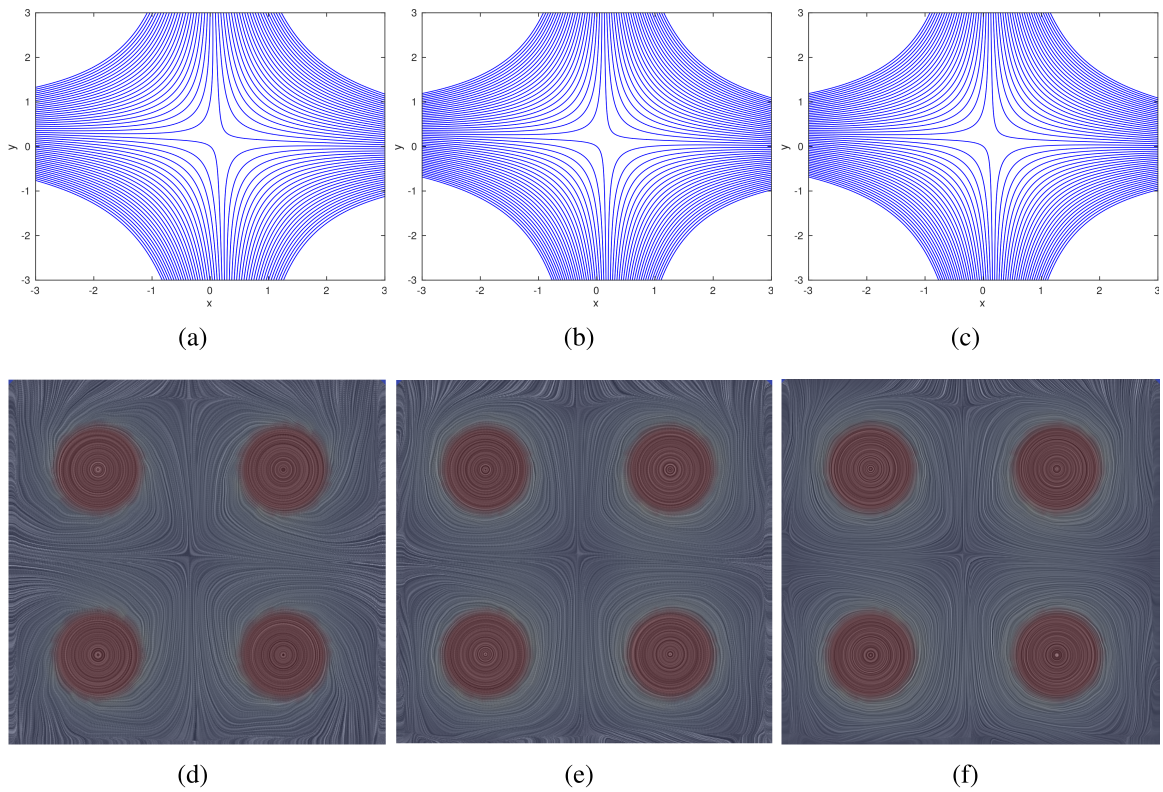

(a) (b) (c)

(d) (e) (f)

Figure 7: Four-roll mill streamlines pattern and LIC visualization using: (a),(d) $\Omega_1 = \Omega_2 = 0.051\ rad/s$ **and** $a = b = 0.9$**. (b),(e)** $\Omega_1 = \Omega_2 = 0.5\ rad/s$ **and** $a = b = 0.4$**. (c),(f)** $\Omega_1 = \Omega_2 = 0.051\ rad/s$ **and** $a = b = 0.4$**.**

However, differently from (Berry and Mackley, 1977), instead of postulating general expression to map catastrophe parameters in angular velocities, we apply a systematic methodology to compute their values. Specifically, we match the speeds $a\Omega_I$, $a\Omega_{II}$ and $a\Omega_{III}$ of the rollers' peripheries to the flow velocities $\mathbf{v}$ calculated by Eq. (11), with the stream function ϕ given by Eq. (6), at the rollers' surface points: $\mathbf{q}_i = (d \cdot \cos(\theta_i), d \cdot \sin(\theta_i))$, with $\theta_i = i \cdot \pi/3$, $i = 0, 1, 2, \ldots, 5$. Therefore, we must solve the linear system:

$$\frac{\partial \phi}{\partial y}(\mathbf{q}_i) = -a\Omega_i \sin(\theta_i), \quad i = 0, 1, \ldots, 5, \tag{40}$$

$$\frac{\partial \phi}{\partial x}(\mathbf{q}_i) = -a\Omega_i \cos(\theta_i), \quad i = 0, 1, \ldots, 5, \tag{41}$$

If we set values for a_1, a_2 and a_3 in Eq. (6), then the Eq. (40)-(41) defines a system with 12 linear equations with just 3 unknowns $(\Omega_I, \Omega_{II}, \Omega_{III})$. Hence, we apply traditional least square technique to find the best 3-upla of angular velocities.

We consider the points p_1, p_2 and p_3 of Fig. 2, in the catastrophe parameter space (a_1, a_2, a_3). The obtained angular velocities are: Point p_1: $\Omega_I = 93.3413\ rad/s$, $\Omega_{II} = 176.5262\ rad/s$, where $\Omega_1 = \Omega_{II}$ and $\Omega_4 = -\Omega_{II}$, $\Omega_{III} = -0.8740\ rad/s$; Point p_2: $\Omega_I = 25.2497\ rad/s$, $\Omega_{II} = 43.7232\ rad/s$, where $\Omega_1 = \Omega_{II}$ and $\Omega_4 = -\Omega_{II}$, $\Omega_{III} = -0.1775\ rad/s$; Point p_3: $\Omega_I = 88.2363\ rad/s$, $\Omega_{II} = 177.6151\ rad/s$, where $\Omega_1 = \Omega_{II}$ and $\Omega_4 = -\Omega_{II}$, $\Omega_{III} = -0.9833\ rad/s$. The corresponding topological changes when passing through points p_1, p_2, p_3 are pictured on Fig. 3. We perform numerical simulation of the setup represented on

Fig. 4.(c), using the obtained angular velocities.

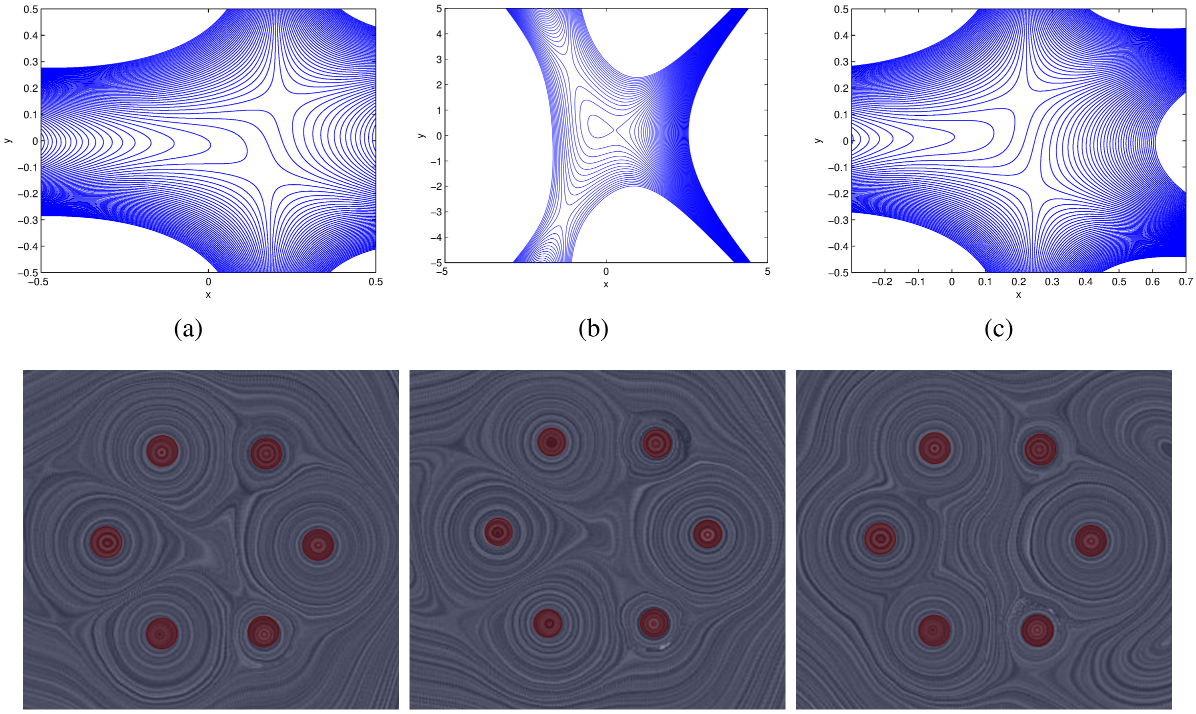

(a) (b) (c)

(d) (e) (f)

Figure 8: Streamline patterns and LIC visualization for: (a)-(d) Point p_1. (b)-(e) Point p_2. (c)-(f) Point p_3.

The polynomials obtained by fitting the model defined by Eq. (37) to the flows through the least square solution of the Eq. (38) are reported in Table 1. The corresponding flow patterns are pictured on Fig. 8.(a)-(c). The comparison between the coefficients in Table 1 and the corresponding catastrophes, given by Eq. (6) with (a_1, a_2, a_3) defined by the points p_1, p_2, p_3, respectively, does not show a direct map between them. For points p_1 and p_3 the singularities of the fitting and catastrophe polynomials are of the same type, as shown in Table 1. So, we expect an equivalence from the topological viewpoint. The streamlines patterns pictured on Fig. 8.(a)-(c) support this claim. However, for point p_2 the patterns of the flows do not match each other, as we observe through Fig. 3.(b) and Fig. 8.(b). On the other hand, the LIC visualization and the flow generated by the catastrophe family seems to be similar (Fig. 3.(b) and Fig. 8.(e)). The point p_2 belongs to the bifurcation surface and, consequently, the corresponding function has degenerate (non-Morse) critical points. Non-Morse functions are structurally instable (sensitive to small perturbation) as we can numerically demonstrate in this case. To do this, we perform a perturbation of the function $f(x, y, a_1 = 1.0, a_2 = 0.0, a_3 = -0.25)$, computed by Eq. (6) as follows:

$$\widetilde{f}(x, y, b) = f(x, y, a_1 = 1.0, a_2 = 0.0, a_3 = -0.25) + by. \tag{42}$$

We set the new coefficient to $b = 0.0001$ in order to keep the perturbation small enough. The critical points of the $\widetilde{f}(x, y, b)$ are 3 saddles and 1 minimum, like the simulated stream function (second line of Table 1). Therefore, small perturbations changes the topology of critical points of the function $f(x, y, a_1 = 1.0, a_2 = 0.0, a_3 = -0.25)$ given by Eq. (6). As a consequence the fitting process should apply a model with enough robustness to deal with numerical issues ('perturbations'), and to fit the target topology. The model given by Eq. (37) is not able to represent the flow of Fig. 8.(b) with the necessary precision. That is a point to be considered in further works.

Table 1: Coefficients obtained by fitting Eq. (37) to the SPH data.

Polynomials coefficients in Eq. (37) and critical points.								
	Points	b_1	b_2	b_3	b_4	b_5	b_6	
	p_1	-0.3361	2.7031	0.0	-0.6894	-0.0175	0.0366	two saddles
	p_2	-0.1878	0.0942	0.0	0.1147	0.0372	-0.0584	three saddles and one minimum
	p_3	-0.4025	2.8334	0.0	-0.6582	-0.6582	-0.0156	two saddles

We perform the SPH simulation of the fluid using angular velocity and artificial viscosity perturbation, according to Fig. 9. We chose the setup of point p_3 to perform the perturbation. The Fig. 9 shows the obtained streamlines patterns and the LIC visualization. The visual comparison is quite subjective. But when computing the critical points we observe that the topology was preserved. Therefore, small perturbations in the simulation parameters generate perturbed SPH solution but without changing the topology. Besides the comparison between Fig. 4.(f) and Fig. 8.(d) shows similar partners which indicates the correctness of our simulation.

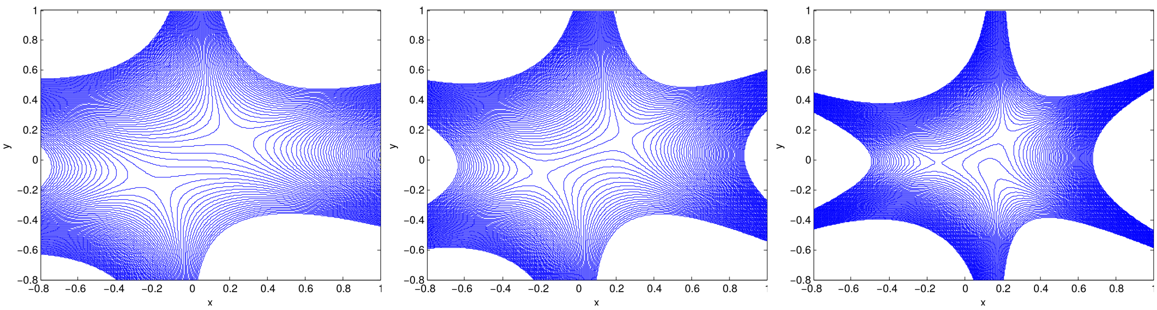

(a) (b) (c)

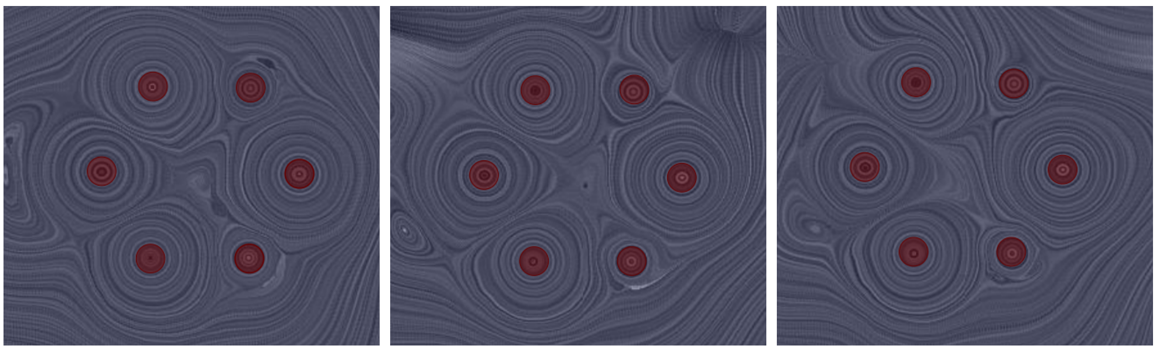

(d) (e) (f)

Figure 9: Six-roll mill streamlines pattern and LIC visualization using: (a),(d) $\overline{\Omega}_1 = 1.1 \cdot \Omega_1$**,** $\overline{\Omega}_2 = 1.1 \cdot \Omega_2$ **and** $\overline{\Omega}_3 = 1.1 \cdot \Omega_3$**. (b),(e)** $\overline{a} = \overline{b} = a - \Delta a$**. (c),(f)** $\overline{\Omega}_1 = 1.1 \cdot \Omega_1$**,**$\overline{\Omega}_2 = 1.1 \cdot \Omega_2$**,** $\overline{\Omega}_3 = 1.1 \cdot \Omega_3$ **and** $\overline{a} = \overline{b} = a - \Delta a$

7 Conclusion and Future Works

In this paper we simulate N-roll mill flows using the SPH technique. The obtained results are analysed from the viewpoint of the Morse and Thom's catastrophe theory. The analysis are supported by quantitative results and visual inspection of the flow patterns.

We revise, by computational experiments, the stability of the Morse flows in the 2 and 4-roll experiments respect to the roll angular velocity and fluid artificial viscosity. The flows that happens for $N = 6$ rolls are studied using the elliptic umbilic catastrophe. We present a procedure to map the parameter space of the catastrophe into angular velocities of the rolls. Then, we perform the simulation of the 6-roll mill apparatus using SPH framework. We compare the numerical solution with the corresponding element of catastrophe family and observed a suitable match from the topological viewpoint in the non-degenerate cases. The structurally instability of degenerate patterns are also discussed and verified the limitations of our model to deal with these cases. Further works are being undertaken to address this problem. Besides, we intend to compute the equivalence between flow patterns and elementary catastrophes as well as to analyze the influence of the catastrophic behavior in numeric and dynamic elements of SPH model.

REFERENCES

Kazuyuki Aihara and Hideyuri Suzuki, 2010. Application of cusp catastrophe theory to reliability analysis of slopes in open-pit mines. *Phil. Trans. R. Soc. A*, vol. 368, pp. 48934914.

B Ataie-Ashtiani and Leila Farhadi, 2006. A stable moving-particle semi-implicit method for free surface flows. *Fluid Dynamics Research*, vol. 38, n. 4, pp. 241.

Jan Awrejcewicz and Vadim Anatolevich, 2008. *Chaos in Structural Mechanics*. John Wiley & Sons.

M. V. Berry and M. R. Mackley, 1977. The six roll mill: unfolding an unstable persistently extensional flow. *Phil. Trans. R. Soc. A*, vol. 287, n. 1337, pp. 1–16.

J. Bonet and T.-S.L. Lok, 1999. Variational and momentum preservation aspects of smooth particle hydrodynamic formulations. *Computer Methods in Applied Mechanics and Engineering*, vol. 180, n. 1–2, pp. 97–115. ISSN 0045-7825. doi: 10.1016/S0045-7825(99)00051-1.

DG Crowley, FC Frank, MR Mackley, and RG Stephenson, 1976. Localized flow birefringence of polyethylene oxide solutions in a four roll mill. *Journal of Polymer Science: Polymer Physics Edition*, vol. 14, n. 6, pp. 1111–1119.

R. Gilmore, 1981. *Catastrophe Theory for Scientists and Engineers*. John Wiley & Sons.

R.A. Gingold and J.J. Monaghan, 1977. Smoothed particle hydrodynamics: theory and application to non-spherical stars. *Mont. Not. of the Royal Astron. Soc.*, vol. 181, pp. 375–389.

V. Girault and P.-A Raviart, 1986. *Finite Element Methods for Navier-Stokes Equations: Theory and Algorithms*. Springer-Verlag.

Amy Henderson and Jim Ahrens, 2004. *The Paraview guide : a parallel visualization application*. Kitware, Inc., New York. ISBN 1-930934-14-9.

Christopher P Hills, 2002. Flow patterns in a two-roll mill. *The Quarterly Journal of Mechanics and Applied Mathematics*, vol. 55, n. 2, pp. 273–296.

C. Hirsch, 1988. *Numerical Computation of Internal and External Flows: Fundamentals of Numerical Discretization*. John Wiley & Sons.

Kyung Sung Kim, Moo Hyun Kim, and Jong-Chun Park, 2014. Development of moving particle simulation method for multiliquid-layer sloshing. *Mathematical Problems in Engineering*pp. 13.

Y. Kun, W. Tongxu, and MA Zhitao, 2010. Application of cusp catastrophe theory to reliability analysis of slopes in open-pit mines. *Mining Science and Technology (China)*, vol. 20, n. 1, pp. 71–75.

G.R. Liu and B. Liu, 2003. *Smoothed Particle Hydrodynamics: A Meshfree Particle Method*. World Scientific. ISBN 9789812564405.

M.B. Liu, G.R. Liu, and K.Y. Lamb, 2003. Constructing smoothing functions in smoothed particle hydrodynamics with applications. *Journal of Computational and Applied Mathematics*, vol. 155, .

Andrea Loi and Stefano Matta, 2011. Catastrophes minimization on the equilibrium manifold. *Journal of Mathematical Economics*, vol. 47, n. 4, pp. 617–620.

J. J. Monaghan, 2012. Smoothed particle hydrodynamics and its diverse applications. *Annual Review of Fluid Mechanics*, vol. 44, n. 1, pp. 323–346.

J.J. Monaghan, 1992. Smoothed Particle Hydrodynamics. *Annual review of astronomy and astrophysics*, vol. 30, pp. 543–74.

Joseph P. Morris, Patrick J. Fox, and Yi Zhu, September 1997. Modeling low reynolds number incompressible flows using sph. *J. Comput. Phys.*, vol. 136, n. 1, pp. 214–226. ISSN 0021-9991. doi: 10.1006/jcph.1997.5776.

T. Poston and I. Stewart, 1978. *Catastrophe Theory and Its Applications*. Pitman.

S.H. Strogatz, 2007. *Nonlinear Dynamics And Chaos*. Studies in nonlinearity. Sarat Book House. ISBN 9788187169857.

Takashi Tamaki, Takashi Torii, and Kei-ichi Maeda, Jul 2003. Stability analysis of black holes via a catastrophe theory and black hole thermodynamics in generalized theories of gravity. *Phys. Rev. D*, vol. 68, pp. 024028.

R. Thom, 1975. *Structural stability and morphogenesis: an outline of a general theory of models*. New York: Benjamin.